GDCh

Research Articles

Angewandte
Chemie
International Edition
www.angewandte.org

Hydroformylation

Rhodium Single-Atom Catalyst Design through Oxide Support Modulation for Selective Gas-Phase Ethylene Hydroformylation

*Marcos G. Farpón, Wilson Henao, Philipp N. Plessow, Eva Andrés, Raúl Arenal, Carlo Marini, Giovanni Agostini, Felix Studt, and Gonzalo Prieto**

Abstract: A frontier challenge in single-atom (SA) catalysis is the design of fully inorganic sites capable of emulating the high reaction selectivity traditionally exclusive of organometallic counterparts in homogeneous catalysis. Modulating the direct coordination environment in SA sites, via the exploitation of the oxide support's surface chemistry, stands as a powerful albeit underexplored strategy. We report that isolated Rh atoms stabilized on oxygen-defective SnO_2 uniquely unite excellent TOF with essentially full selectivity in the gas-phase hydroformylation of ethylene, inhibiting the thermodynamically favored olefin hydrogenation. Density Functional Theory calculations and surface characterization suggest that substantial depletion of the catalyst surface in lattice oxygen, energetically facile on SnO_2, is key to unlock a high coordination pliability at the mononuclear Rh centers, leading to an exceptional performance which is on par with that of molecular catalysts in liquid media.

Introduction

The stabilization of isolated metal atoms, while controlling their direct chemical environment, is central to the high modulability, mechanistic specificity, and conversion selectivity inherent to catalysis by enzymes and organometallic complexes in solution. Achieving a similar active site design with catalytic metals dispersed on thermally and chemically stable oxide carriers has long stood as a major research goal. In recent years, a surge of interest has focused on oxide-supported single-atom catalysts (SACs).[1–4] SACs hold the promise to integrate the monoatomicity and simplified site architecture of organometallic catalysts with the technically advantageous properties of solid catalysts, thus helping bridge the classically dichotomic realms of homogeneous and heterogeneous catalysis. Major research efforts have concentrated on developing routes to stabilize isolated metal centers on oxides,[5–8] increasing the metal loading at which atomic dispersion is feasible,[9–11] and assessing differences in performance with metal aggregates.[12–15]

Next to metal identity, the oxide support offers ample, although hitherto less explored, possibilities for active site engineering in SACs. Even in classical supported metal catalysts bearing polyatomic metal ensembles (clusters or nanoparticles), the oxide support is an essential design variable. Through strong metal-support interactions,[16,17] electronic modifications or the provision of additional sites at the metal-oxide interface,[18–20] supports can profoundly impact catalytic performance. This is only accentuated in SACs, wherein all metal atoms directly interface with the oxide carrier, and the latter acts as an inorganic ligand, providing anchoring sites[21] and potentially adjusting the electronic properties of the metal centers.[22,23] Understanding, as a first step towards exploiting, cooperative effects exerted by oxide supports represents a powerful approach to design all-inorganic SACs as solid replacements for their molecular counterparts in processes conventionally pertaining to homogeneous catalysis.

A major example is the hydroformylation (HF) of olefins to aldehydes with syngas (H_2/CO).[24] SACs based on Rh

[*] M. G. Farpón, W. Henao, E. Andrés, Dr. G. Prieto
ITQ Instituto de Tecnología Química, Universitat Politècnica de València-Consejo Superior de Investigaciones Científicas (UPV-CSIC)
Av. Los Naranjos s/n, 46022 Valencia (Spain)
E-mail: prieto@itq.upv.es

Dr. P. N. Plessow, Prof. Dr. F. Studt
Institute of Catalysis Research and Technology (IKFT), Karlsruhe Institute of Technology (KIT)
Hermann-von-Helmholtz Platz 1, 76344 Eggenstein-Leopoldshafen (Germany)

Dr. R. Arenal
Laboratorio de Microscopias Avanzadas (LMA), Universidad de Zaragoza
Mariano Esquillor s/n, 50018 Zaragoza (Spain)

and
Instituto de Nanociencia y Materiales de Aragón (INMA), CSIC-Universidad de Zaragoza
Pedro Cerbuna 12, 50009 Zaragoza (Spain)
and
ARAID Foundation
50018 Zaragoza (Spain)

Dr. C. Marini, Dr. G. Agostini
ALBA Synchrotron Light Source
Carrer de la Llum 2–26, Cerdanyola del Vallès, Barcelona (Spain)

have shown to be effective catalysts in liquid phase, reaching turnover frequencies (TOF) comparable to those attained with molecular catalysts in solution.[25–28] Frequently, however, leaching of metal species into solution, which translates into potential contributions from homogeneously catalyzed pathways and net metal losses, remains a major concern. Therefore, particularly for light (C_2–C_4) olefins, the development of a gas-solid heterogeneous catalyzed HF process is associated to several process design incentives. Next to olefin valorization via oxo-functionalization, gas-phase HF is also attractive as a reactive separation, alternative to energy-intensive cryogenic distillation, to recover ethylene from mixtures with low added-value alkanes, e.g. in ethane cracker or refinery off-gases.[29,30] However, this process faces important challenges, particularly attaining high hydroformylation selectivity by inhibition of the thermodynamically favored hydrogenation path to ethane.

Various families of solid catalysts have been explored for the gas-phase hydroformylation of ethylene. These include solid-tethered Rh complexes,[31] Rh clusters stabilized in zeolites,[25] and supported Rh-based bimetallics[32] and phosphide[33] nanoparticles. However, comparatively lower selectivities to propanal than those within reach for homogeneous catalysis have been systematically observed.[34] These limitations of all-solid catalysts brought the attention onto supported ionic liquid phase (SILP) catalysts, wherein a free molecular HF catalyst operates dissolved in a non-volatile ionic liquid supported on a solid carrier.[35] Excellent TOF (>100 h^{-1}) and enhanced selectivities (90–100 %) have been demonstrated via the elegant SILP approach.[36,37] Nevertheless, the technically demanding handling of the supported liquid phase, sluggish intraparticle mass transport and catalyst deactivation driven by accumulation of oxygenate products in the liquid overlay remain as technical challenges.[34]

Herein we report that monatomic Rh sites stabilized on oxygen-defective SnO_2 are all-inorganic catalysts which combine excellent TOF with full selectivity in the gas-phase hydroformylation of ethylene, an exceptional catalytic performance which is on par with that of molecular catalysts in liquid media.

Results and Discussion

Rhodium single-atom catalysts (SACs) have been synthesized by the oxidative metal dispersion and atom trapping route introduced by Datye and co-workers[5] on monoclinic (m)-ZrO_2, CeO_2 and SnO_2 oxides at a surface-specific metal content of 1.0 ± 0.1 Rh$_{at}$ nm^{-2} (Table S1).[13,38] The set of MO_2 oxide support materials has been selected to share the cation M valency while spanning a wide range of surface oxygen vacancy formation energies [E(O_{vac})] (Figure 1).

Oxygen vacancies have been proposed to play decisive roles in the genesis of active catalytic centers in SACs.[40,41] Therefore, E(O_{vac}) prospectively is an important screening parameter to assess support modulation effects on single-atom catalysts.
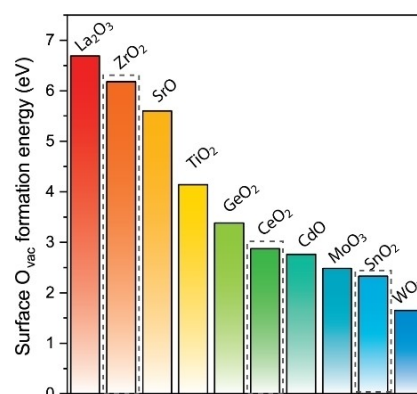
Figure 1. Surface oxygen vacancies (O_{vac}) formation energies for selected metal oxides.[39]

X-ray diffraction did not detect Rh (oxide) crystallites in the as-synthesized catalysts, indicating metal species which lack long-range atomic order (Figure S1). Rhodium atomicity and coordination environment were assessed by X-ray Absorption Spectroscopy (XAS). Figure 2a shows the radial distribution for the Extended X-ray Absorption Fine Structure (EXAFS) spectra. The corresponding spectral Continuous Cauchy Wavelet Transforms (CCWT) are given in Figure 2b. Modulus signals at radial distances of ca. 1.6 Å, corresponding to Rh–O coordination, dominate the spectra. No signs for neither Rh–Rh coordination, expected at radial distances of ca. 2.4 Å, nor 2nd-shell Rh–O–Rh (ca. 3 Å) are registered, in agreement with the absence of metal (oxide) aggregates. For Rh$_1$/SnO$_2$, an additional broad scattering contribution centered around 3.4 Å, is ascribed to tin cations at the 2nd coordination shell around isolated Rh atoms.[42] Density Functional Theory (DFT)-optimized models for isolated Rh atoms isomorphically substituted on the topmost oxide surface provided a physically sensible fit of the experimental EXAFS spectra in all cases (see section 3 in the Supporting Information). Moreover, consideration of additional Rh–Rh or Rh–O–Rh scattering paths, as in metal (oxide) aggregates, led to either poorer or directly physically nonsensible descriptions of the experimental data. In agreement with XAS results, Aberration Corrected High-Angle Scanning-Transmission Electron Microscopy (AC-HAADF-STEM) showed no evidence of metal aggregates on the catalysts surface (Figure 2c). Through local Z-contrast analysis on the micrographs,[43–45] isolated Rh atoms within columns of Zr atoms are discernible on ZrO$_2$. For Rh$_1$/CeO$_2$ and Rh$_1$/SnO$_2$, the higher Z-contrast associated to Sn ($Z_{Sn} = 50$) and Ce ($Z_{Ce} = 58$) atoms, compared to Rh ($Z_{Rh} = 45$), impedes direct visualization of single Rh atoms. On the same high-Z supports, AC-HAADF-STEM proved adequate to identify rhodium oxide aggregates which developed only on comparative catalysts with higher Rh contents (Figure S2), supporting the absence of metal oxo-aggregates on Rh$_1$/CeO$_2$ and Rh$_1$/SnO$_2$. Complementarily, these results provide compelling support for the stabilization of single Rh atoms on the three oxide supports.
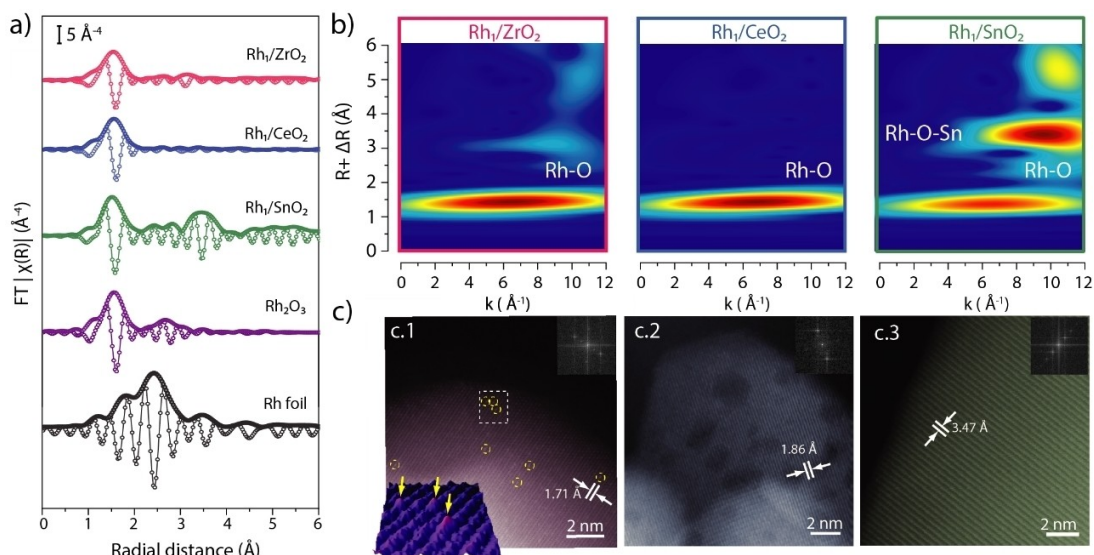
Figure 2. Structural analysis of Rh single-atom catalysts on different oxide support materials. a) Fourier Transform of the k^3-weighted EXAFS function (no phase correction) and b) Continuous Cauchy Wavelet Transforms of the EXAFS function for the series of as-synthesized Rh_1/MO_2 catalysts (M = Zr, Ce, Sn). For reference purposes, data for Rh_2O_3 (dispersed on carbon) and a metallic Rh foil are also included on panel (a). The spectra were collected at room temperature under He for the as-synthesized catalysts, i.e. following Rh incorporation on the oxide supports and oxidative metal dispersion in air at 1073 K. c) Representative AC-HAADF-STEM images. Insets (top-right) show the Fast Fourier-Transform function applied to determine the crystal *d*-spacings indicated on the micrographs, which correspond to the (2 0 2) plane in m-ZrO_2 (c.1), (2 2 0) in CeO_2 (c.2) and (1 1 0) in SnO_2 (c.3), respectively. On panel (c.1) isolated Rh atoms have been marked by the dashed yellow circles included as a guide to the eye. The corresponding 3D map of Z-contrast for the region marked on the micrograph is also given, wherein the arrows point to the atomic-size high-Z-contrast objects ascribed to isolated Rh atoms.

For reference purposes, a Rh/SiO_2 material was also synthesized by dispersing Rh on SiO_2. For this catalyst, both XAS and AC-HAADF-STEM results showed the formation of polynuclear Rh_n aggregates, even at a comparatively lower surface-specific metal loading of 0.4 Rh_{at} nm^{-2} (Figure S3). This is ascribed to the –OH surface termination and poor reducibility of silica, an oxide with a stronger covalent character, which lacks effective sites for the trapping of Rh atoms during oxidative dispersion treatments. X-ray Photo-emission Spectroscopy (XPS) showed Rh3d core-level Binding Energies (BE) consistent with oxidic species, i.e. $Rh^{\delta+}$ ($\delta = 3$–4),[46] regardless of the identity of the oxide support (Figure S4). The stability of the isolated Rh atoms against reductive agglomeration was studied by in situ temperature-programmed reduction monitored by X-Ray Absorption Near-Edge Structures spectroscopy (XANES-TPR). As shown in Figure 3a, exposure to a flow of 20 %H_2/He at increasing temperatures in the 298–773 K range led, in all cases, to a progressive dampening of the white line alongside a down-shift of the absorption edge energy (E_0), both indicative of Rh reduction. The observation of isosbestic points at 23.246 keV and 23.263 keV in the temperature-resolved spectra collection suggests a one-to-one transformation from a single oxidic Rh species to Rh^0. Further insights into the evolution of the XANES spectra emerged from a least-squares linear combination analysis (LS-LCA) (see Figure S5 for details). As shown in Figure 3b, the onset temperature for the reduction of Rh species was the lowest for Rh_n/SiO_2, underscoring the limited capacity of SiO_2 to stabilize monoatomic metal species. The reduction kinetics for the series of SACs scaled in the order

$Rh_1/CeO_2 > Rh_1/ZrO_2 > Rh_1/SnO_2$, indicative of an opposite order for the stability of the single Rh atoms against reductive agglomeration. Analysis of the EXAFS spectra following the XANES-TPR experiment (Figure S6) consistently showed a decline in the modulus intensity for Rh–O scattering contributions, accompanied by the emergence of Rh–Rh scattering signals as a result of reductive metal agglomeration into polynuclear Rh_n ensembles. The extent of these spectral modifications was the lowest for Rh_1/SnO_2, for which Rh–O and Rh–O–Sn scattering contributions still dominated the spectrum after the in situ reduction, reinforcing the notion that the stabilization of isolated Rh centers is the strongest on SnO_2.

The catalytic performance of the set of Rh SACs was assessed for the gas-phase hydroformylation of ethylene with syngas under relevant operation conditions (H_2:CO:C_2H_4 1:1:1 (vol), 423 K, 20 bar). Control tests with the neat oxide supports showed ca. two orders of magnitude lower activity, discarding any significant contribution to the hydroformylation rates reported for Rh catalysts. All catalysts showed to be active. Besides propanal, minor amounts of 1-propanol and 2-methyl-2-pentenal products were detected as secondary selective hydrogenation and aldol condensation products, respectively, along the HF conversion path. Ethane was produced through the competitive olefin hydrogenation side-reaction. Figure 4a summarizes the catalytic results. Rh_1/CeO_2 and Rh_1/ZrO_2 showed initial TOF rates, per unit Rh atom, in the range of 0.6–1.4 h^{-1}. Selectivity towards HF was similar, in the range of 55–65 mol%, and comparable to those reported in the literature for different solid ethylene hydroformylation
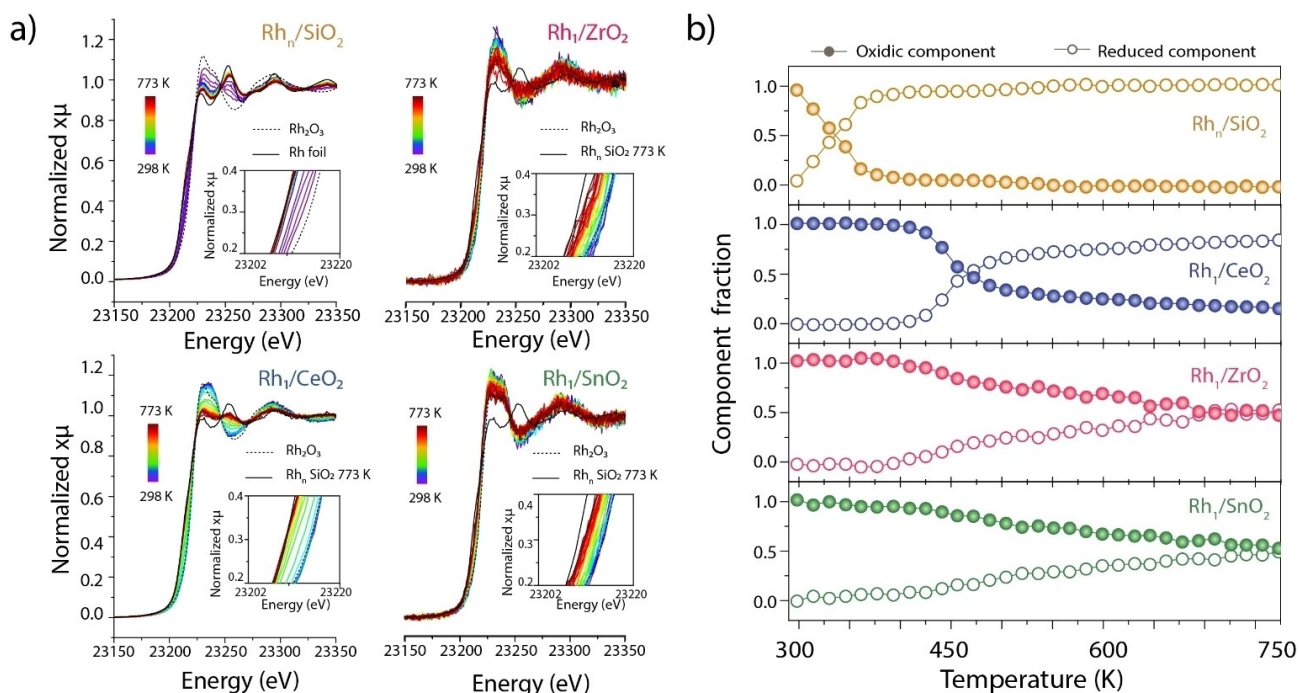
Figure 3. Support-dependent stability of mononuclear metal sites in Rh_1/MO_2 catalysts studied by in situ temperature-programmed reduction monitoredby X-Ray Absorption Near-Edge Structure spectroscopy (XANES H_2-TPR). a) Temperature-resolved XANES spectra for the series of Rh_1/CeO_2, Rh_1/ZrO_2 and Rh_1/SnO_2 single-atom catalysts and the Rh_n/SiO_2 reference catalyst recorded in situ during the exposure of the catalysts to flow of $20\%H_2/He$ at increasing temperatures in the range of 298–773 K with a heating rate of 5 $K\,min^{-1}$. The corresponding spectra for Rh_2O_3 (dispersed on carbon) and Rh_n/SiO_2 after reduction at 773 K, are also included as reference components for fully oxidic and fully reduced Rh species, respectively (in the case of Rh_n/SiO_2, panel a, the spectrum for a metallic Rh foil is included instead). The insets show a close-up view around the inflection point of the absorption edge to better perceive edge energy shifts as a function of the treatment temperature under flow of $20\%H_2/He$. b) Evolution of the oxidic (starting) and metallic Rh contributions with temperature, as determined via a Least-squares Linear Combination Analysis (LS-LCA). See Experimental methods and Figure S5 in the Supporting Information for further information on the fitting procedure.
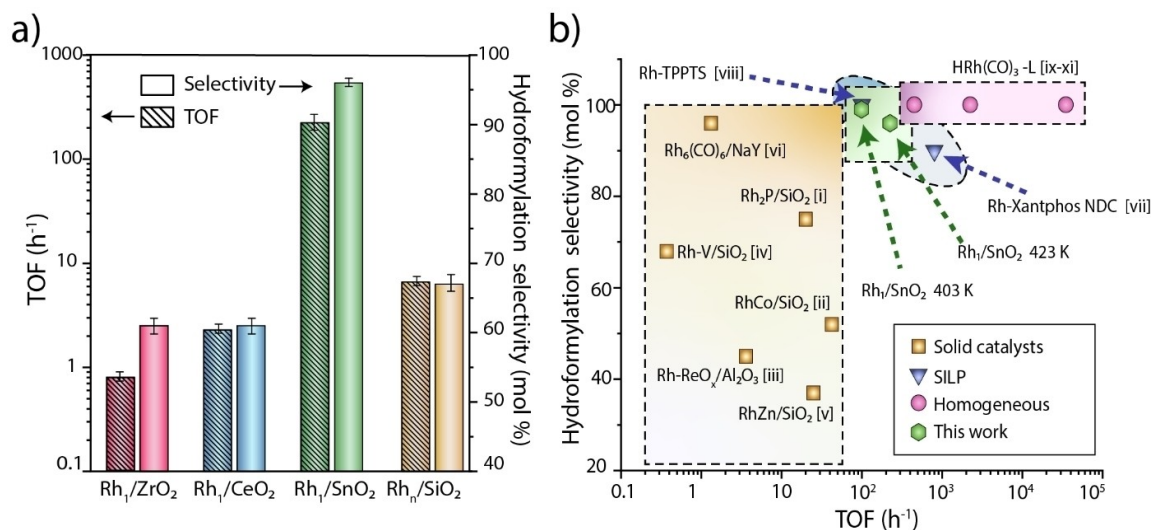
Figure 4. Gas-phase hydroformylation of ethylene. a) Initial ethylene hydroformylation turnover frequency TOF and selectivity for single-atom catalysts supported on the series of MO_2 supports (M = Zr, Ce, Sn). The performance of a reference Rh_n/SiO_2 catalyst has also been included for comparison. Reaction conditions: gas feed $Ar:CO:H_2:C_2H_4$ $1/5:1:1:1$ (vol), $T = 423$ K, $P = 20$ bar. b) Comparison of the catalytic performance for the Rh_1/SnO_2 single-atom catalyst (this work) with the state-of-the-art, including homogeneous catalysts (organometallic complexes in solution), organometallic complexes in supported ionic liquid-phase (SILP) catalysts and all-solid catalysts reported in the literature (see Table S2 in the Supporting Information for further details).

catalysts.[47,48] A comparatively higher HF rate (3.7 h^{-1}) and selectivity (68%) were determined for the reference Rh$_n$/SiO$_2$, which fall also in the range of previously observed performances for oxide-supported Rh catalysts. In stark contrast, Rh$_1$/SnO$_2$ showed a hydroformylation TOF of 225 h^{-1}, i.e. more than two orders of magnitude higher than for the CeO$_2$- and ZrO$_2$-supported SAC analogues. More singularly, this outstanding reaction rate was combined with a HF selectivity >95%. This selectivity increased further to >99% at a milder reaction temperature of 403 K, while retaining a hydroformylation TOF >100 h^{-1}. Notably lower HF rates were observed for comparative Rh$_n$/MO$_2$ (M=Zr, Ce, Sn) bearing Rh nanoparticles, illustrating the benefits of the maximum Rh site exposure attained at single-atom dispersion (Figures S7 and S8). As illustrated in Figure 4b, to our knowledge, the performance of the Rh$_1$/SnO$_2$ single-atom catalyst is unprecedented for all-solid catalysts and indeed comparable to those offered by molecular organometallic catalysts operating in liquid environments, either in solution or dissolved in the liquid overlay on SILP catalysts.

The resting state of the Rh species during and following exposure to ethylene HF reaction conditions at 423 K was studied by operando X-ray absorption spectroscopy and in situ Fourier-Transform infrared spectroscopy (FTIR). Due to safety limitations, reaction experiments in the spectroscopic cells were performed at a total pressure of 8 bar. Control tests showed that effectively identical performance (TOF, selectivity) trends among the series of SACs held at this comparatively lower pressure (Figure S9). EXAFS spectra recorded after reaction in situ were consistent with isolated Rh centers (Figure S10). For Rh$_1$/ZrO$_2$ and more clearly for Rh$_1$/CeO$_2$, next to the predominant Rh–O scattering, a very incipient contribution potentially attributable to Rh–Rh scattering could be discerned. Thus, the formation of a small fraction of Rh nanoclusters cannot be completely ruled out, in accordance with the poorest stability exhibited by Rh$_1$/CeO$_2$ against Rh agglomeration under reducing conditions. Moreover, no Rh aggregates could be detected with AC-HAADF-STEM following the reaction (Figure S11). Therefore, single-atom sites are largely preserved during exposure to ethylene HF conditions at 423 K.

The nature of the surface-exposed Rh sites was studied with FTIR using CO as a surface probe molecule, following in situ exposure to ethylene HF conditions. A temperature of 133 K was selected to avoid oxidative disruption phenomena, which CO is known to promote on small Rh clusters at higher temperatures,[49] ensuring the preservation of Rh speciation set after exposure to reaction conditions. As shown in Figure 5, sharp bands emerged in the range of 2100–2300 cm^{-1}, which developed with increasing CO coverage. These bands are associated to the υ(C–O) stretching vibration of CO adsorbed on coordinatively unsaturated (cus) Zr, Ce and Sn Lewis sites, and surface OH groups, exposed on the surface of the oxide supports.[50] Moreover, in all cases, doublets were observed already from the incipient CO doses, peaking at 2013/2088 cm^{-1} for Rh$_1$/ZrO$_2$, 2009/2082 cm^{-1} for Rh$_1$/CeO$_2$, and 2017/2085 cm^{-1} for Rh$_1$/SnO$_2$, respectively. Their doublet nature and insensitivity to CO coverage enables to unambiguously assign these signals to the antisymmetric and symmetric υ(C–O) stretching, respectively, in Rh geminal dicarbonyl species.[51] Noticeably, the latter bands appear less defined in the case of Rh$_1$/SnO$_2$, suggesting a lower abundance on the catalyst surface. The detection of dicarbonyls as the dominant Rh species, alongside the absence of distinct contributions from neither linear (atop) nor bridged-bonded CO on Rh aggregates, indicate the predominance of atomically dispersed Rh in all cases. Collectively, XAS, STEM and FTIR results furnish evidence for the persistence of mononuclear Rh species under ethylene hydroformylation conditions at 423 K, regardless of the identity of the oxide support.

The screening of reaction temperatures in the range of 423–473 K revealed a generalized progressive decrease in the selectivity to hydroformylation with increasing temperature (Figure S12b). Based on the HF rates determined in this temperature range, apparent activation energies (E_{app}) of 76 and 50 kJ mol^{-1} were obtained for ethylene HF on Rh$_1$/ZrO$_2$ and Rh$_1$/CeO$_2$, respectively (Figure S13). Higher
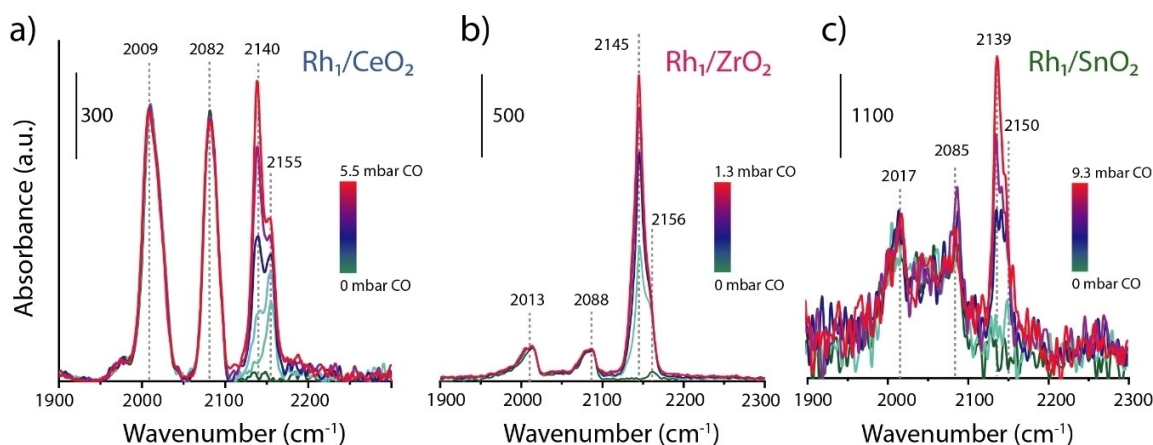
Figure 5. Resting state of surface Rh species in Rh$_1$/MO$_2$ single-atom catalysts. Fourier-Transform transmission infrared spectra recorded after stepwise CO dosage on a) Rh$_1$/CeO$_2$, b) Rh$_1$/ZrO$_2$ and c) Rh$_1$/SnO$_2$ SACs at 133 K following in situ exposure to ethylene hydroformylation reaction conditions (CO:H$_2$:C$_2$H$_4$=1:1:1 vol, T=423 K, P=8 bar). On the y-axis, absorbance has been normalized per unit mass of rhodium.

values in the range of 88–95 kJ mol^{-1} were determined for ethylene hydrogenation (Figure S14). These reaction barriers are accordant with those found previously for alternative solid Rh catalysts.[32] Consistent values were also determined for Rh$_n$/SiO$_2$ under identical conditions. For these catalysts, restoring a milder reaction temperature of 443 K, after operation at 473 K, i.e. the highest reaction temperature in the range inspected, evidenced a permanent activity loss of 18–63 % (Figure S12a). However, the original selectivity pattern at 423 K could be substantially restored, within ±4 % (Figure S15). These findings suggest that active centers enduring the higher reaction temperature largely preserve their intrinsic behavior.

Once again, Rh$_1$/SnO$_2$ departed markedly from the above general trend. Increments in reaction temperature above 423 K led to a progressive deactivation, so conspicuous that it eventually inverted the slope in the corresponding Arrhenius plot, obscuring the assessment of a true E_{app} (Figure S13). Moreover, restoring a reaction temperature of 443 K, after operation at 473 K, failed to recover the original product pattern, and an obvious drop was observed in the selectivity to the HF path from 91 % to 53 %. These findings prompted us to analyze the deactivation behavior of this catalyst in greater detail. At a milder reaction temperature of 383 K, Rh$_1$/SnO$_2$ showed an initial transient period, characterized by a rising activity, likely as a result of the in situ genesis of HF sites (Figure S16). This activation was followed by a significant stability for at least 85 h on-stream, remarkably alongside >97 % selectivity to propanal, which renders Rh$_1$/SnO$_2$ an exceptional catalyst for the gas-phase hydroformylation of ethylene. At higher reaction temperatures, particularly at ≥423 K, a fast activity decline occurred from the onset of the reaction (Figure S16). These results underscore that the exceptionally selective HF sites stabilized on Rh$_1$/SnO$_2$ are more susceptible to irreversible deactivation at high operation temperatures.

To gain further molecular-level insights into the remarkable performance exhibited by Rh$_1$/SnO$_2$, DFT calculations were performed at the PBE-D3 level of theory.[52,53] Calculations were performed with the projector augmented wave (PAW) method[54] using VASP in version 5.4.1 and a cutoff of 400 eV for the expansion of the bands in plane waves. All calculations were performed with closed-shell occupation, since test calculations did not indicate spin-polarization. Gibbs free energies were obtained using the harmonic approximation based on a numerical partial Hessian, which includes the Rh atom and all adsorbates including the two closest lattice oxygens, which also act as ligands for the Rh-complex. Full details on the computational methodology are provided in the Supporting Information. Cartesian atomic coordinates and computed frequencies are provided in the Supporting Information document *Computational Structures.*

To model the tin oxide support, we considered the most stable SnO$_2$(110) facet. Different levels of reduction of this surface were studied computationally, varying the density of oxygen vacancies[55] and including surface reconstructions which require the diffusion of Sn out of its lattice positions.[56] The standard reaction enthalpy for tin (IV)

oxide reduction according to $SnO_2 + 2CO \rightarrow Sn + 2CO_2$ is $\Delta H° = 11.67$ kJ mol^{-1}. Under the notably reducing ethylene HF reaction conditions studied herein, i.e. $T = 423$ K, $P_{CO} = 6.2$ bar and very low CO_2 partial pressures, the equilibrium is far on the side of elemental Sn. However, since the formation of Sn^0 is not observed experimentally, we conclude that SnO$_2$ reduction is hindered kinetically. We, therefore, have considered only partial reduction extents for the SnO$_2$(110) surface, through the formation of oxygen vacancies, without further reconstruction. Complete removal of all surface oxygen atoms, as also considered in previous work,[57] is thermodynamically viable under the HF conditions. However, while we found free energy barriers of up to 104 kJ mol^{-1} for the removal of *bridging* oxygen atoms, by reaction with CO, a higher barrier of 154 kJ mol^{-1} needs to be surmounted for further reduction through abstraction of *in-plane* oxygen atoms, which should not be accessible under the reaction conditions considered ($T = 423$ K). We have therefore studied ethylene HF at site models based on a SnO$_2$(110) surface, following depletion of all *bridging* oxygen atoms, i.e. 1/3 of the total surface oxygen.

On the stoichiometric SnO$_2$(110) surface, two inequivalent sites could be identified for substitution of Sn by Rh, i.e. the coordinatively unsaturated (*cus*) site (site I), which remains five-fold coordinated and the initially six-fold coordinated site II. The latter was found to be more stable under dry oxidative conditions (Section 2 in the Supporting Information), and hence expected to be favored at the high-temperature oxidative dispersion conditions applied to synthesize the Rh$_1$/SnO$_2$ SAC. Following the loss of *bridging* surface O, this Rh site turns four-fold coordinated and provides two free coordination sites. Consistently, EXAFS revealed a decrease in the Rh–O average coordination number (CN) from 5.1 to 4.1, following in situ exposure to ethylene HF conditions at 423 K (Figure S17). Hence, the experimental data are coherent with the O-depletion at the Rh coordination sphere in the proposed site model, which we therefore chose for our mechanistic investigations.

As shown in Figure 6, CO binds strongly to the two vacant sites on the Rh center, with adsorption energies of −231 and −98 kJ mol^{-1}, respectively, forming the stable dicarbonyl complex **a**. Although Rh is now again coordinated by six ligands (two CO molecules and four lattice O), the complex can react by detaching from the lattice O at the second oxide layer, remaining coordinated only to two oxygens on the topmost oxide layer. This provides an energetically facile route to a Rh center with an unusually high coordination flexibility.

Hydroformylation by molecular Rh complexes in homogeneous catalysis generally occurs via monohydrides.[58] For Rh SACs, a mechanism starting by Rh dicarbonyls reacting with H$_2$ to dihydride species has also been proposed.[59] However, we found this mechanism not to be favorable on the herein considered model. Instead, H$_2$ dissociation at the Rh/oxide interface was favored, with a barrier of 109 kJ mol^{-1}. This led to a monohydride complex (**1**), of similar stability as the initial dicarbonyl complex, with the second H adatom being transferred to the SnO$_2$(110) support. For the Rh hydride dicarbonyl **1**, DFT predicted antisymmetric and symmetric
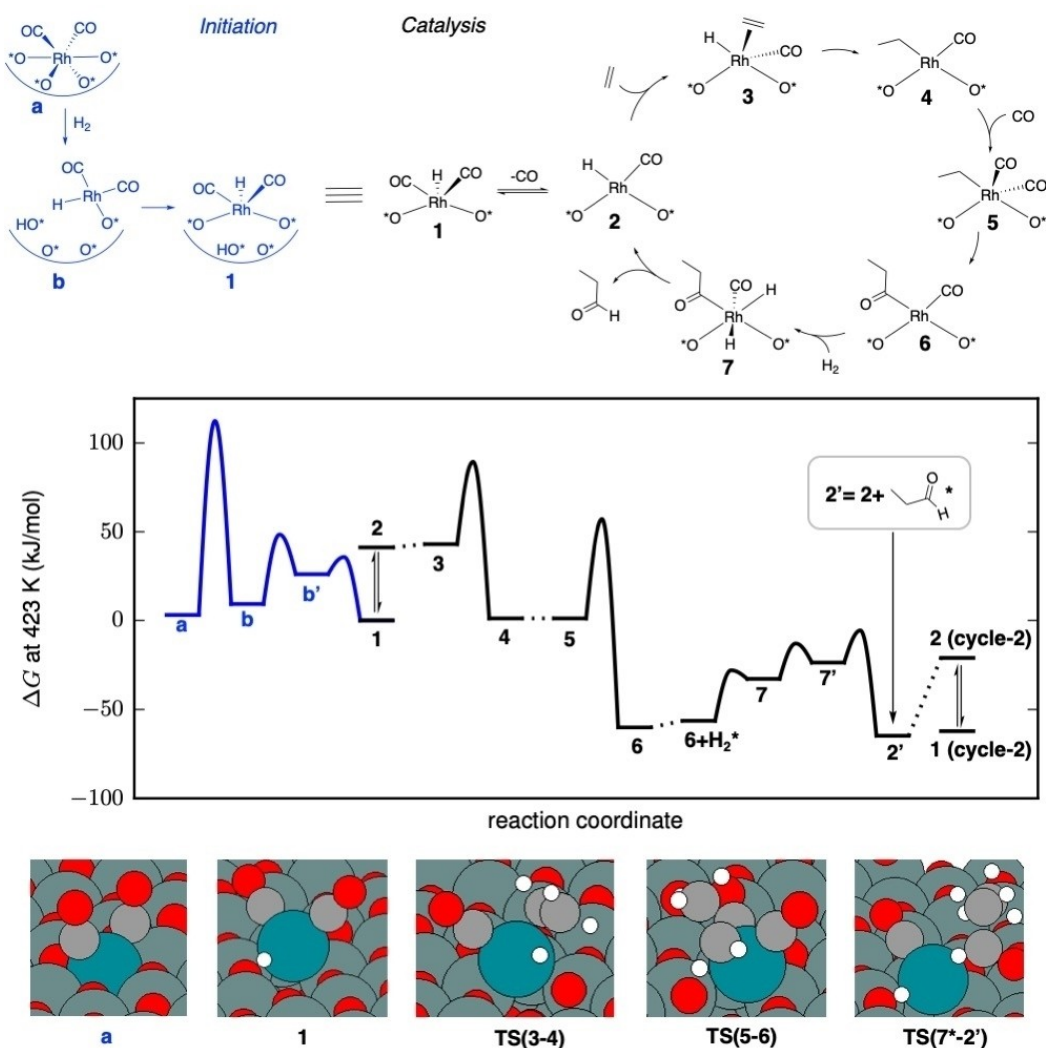
Figure 6. Density functional theory mechanistic calculations. Reaction scheme for initiation through the formation of a Rh monohydride dicarbonyl and for the investigated ethylene hydroformylation catalytic cycle. Free energy diagram for the depicted mechanism at $T = 423$ K and $P_{CO} = H_2 = P_{C_2H_4} = 6.2$ bar reference pressures. Structures resulting from rearrangements or adsorption are not in all cases shown in the scheme and are labeled 7, 7′, etc. The structure of important intermediates and transition states is depicted at the bottom.

C–O stretching frequencies of 2018 and 2066 cm^{-1}, respectively, in fair agreement with the experimental values (Figure 5c). The resulting site structure can then react following a typical Heck-Breslow mechanism, i.e. after CO desorption and ethylene adsorption, insertion of ethylene into the Rh–H bond gives an ethyl group. Following adsorption of an additional CO molecule and migratory insertion, dissociation of H$_2$ and subsequent reductive elimination deliver the final propanal product. The highest barrier is observed for the insertion of ethylene into the Rh–H bond, TS(**3–4**), with a ΔG of 89 kJ mol^{-1} relative to structure **1**, compatible with the experimentally observed high activity. We also studied the alternative hydrogenation reaction path to ethane (see Section 2 in the Supporting Information). The hydrogenation path diverges from that for hydroformylation at intermediate **4**. However, the free energy barrier for hydrogenation (105 kJ mol^{-1}) is much higher than that for the reaction with

CO (57 kJ mol^{-1}), in agreement with the high selectivity towards HF observed experimentally.

Prompted by these DFT predictions, we further investigated O-depletion on SnO$_2$, under reaction conditions, experimentally. Changes in near-surface oxygen speciation were assessed by analyzing the O1s core level in the corresponding XP spectra (Figure S18a). Two different O species could be discerned, with BE of 529.8 and 531.5 eV, associated to O^{2-} in [SnO$_6$] octahedra in the regular SnO$_2$ lattice, and to oxygen in non-stoichiometric local environments, i.e. in the vicinity of oxygen defects (V$_O^0$, V$_O^+$, or V$_O^{++}$), respectively.[60,61] The relative abundance of the two O species may be used as an indirect proxy for the density of O$_{vac}$ on Rh$_1$/SnO$_2$. The O$_{vac}$ density increased significantly on exposure of the catalyst to ethylene HF conditions at increasing temperatures up to 423 K. Further increments in temperature resulted in no additional spectral modifications, suggesting an asymptotic approach to a maximum oxygen

depletion, e.g. as a result of kinetic hindrance. Remarkably, this evolution was paralleled by that of the HF deactivation rate constant, which surged steeply on increasing the reaction temperature up to 423 K, above which it also topped out and became less temperature-dependent (Figure S18b). Moreover, in situ Raman spectroscopy provided consistent results, and further identified *bridging* O_{vac} as those surface defects prevailing at the reaction temperatures for optimal hydroformylation performance, in agreement with DFT predictions (Figure S19). It is therefore inferred that, while a substantial surface O removal is important to develop the exceptional Rh active centers on SnO_2, excessive surface oxide reduction is detrimental and suppresses HF activity.

The deactivation undergone by Rh_1/SnO_2 at higher reaction temperatures is not associated to Rh reductive agglomeration. Indeed, contributions from Rh^0 remained limited at reaction temperatures even up to 503 K, as confirmed by in situ XPS (Figure S20), whilst Rh aggregates could not be detected by AC-HAADF-STEM (Figure S21). As a topmost surface-sensitive method, in situ CO-FTIR provided further insight into surface reduction phenomena. Exposure of Rh_1/SnO_2 to a mild reaction temperature of 383 K, at which the catalyst is particularly selective and stable (Figure S16), led to the observation of an intense and well-defined band doublet, at 2021 and 2090 cm^{-1}, for $RhH(CO)_2$ species (Figure S22). Increasing the reaction temperature to which Rh_1/SnO_2 had been exposed, prior to CO-FTIR probing, led to the gradual decline of these bands into a noisy and ill-defined spectral background, to become undetectable after reaction at 503 K. Even the IR band at ca. 2140 cm^{-1} vanished almost completely, indicating a very limited availability of $Sn^{\delta+}$ Lewis centers on the surface. Collectively, these observations substantiate an excessive reduction of the SnO_2 surface, i.e. removal of lattice O, at reaction temperatures higher than ca. 423 K, which is clearly detrimental for HF catalysis. Interestingly, deactivation is reversible. Activity is restored to a substantial extent, alongside essentially full selectivity to propanal, upon the replenishment of surface O by in situ exposure to air at 383 K (Figure S23). Hence, our results emphasize the remarkable stability of monoatomic Rh centers on Rh_1/SnO_2. Moreover, they signify the importance of modulating the density of surface oxygen vacancies to achieve a high coordination pliability at the Rh centers, while preventing an excessive metallic character of the catalyst surface, to attain the exceptional ethylene hydroformylation performance.

Conclusion

Engineering the energetics of surface oxygen vacancy formation on oxide supports is a powerful strategy towards the rational modulation of Single-Atom Catalysts (SACs). The stabilization of mononuclear Rh sites on SnO_2 leads to a SAC with exceptional performance for the gas-phase hydroformylation of ethylene. At a reaction temperature of 403 K, excellent TOF ($>100\ h^{-1}$) is harmonized with unprecedented selectivity (99 %). Surface spectroscopic characterization and DFT calculations reveal that an energetically facile and substantial depletion of the SnO_2 surface

in oxygen is key to develop Rh sites with high coordination flexibility and excellent hydroformylation activity. However, excessive oxide surface reduction, at higher operation temperatures, is detrimental for catalysis. The Rh_1/SnO_2 SAC attains performance indicators commensurate to those thus far exclusive of molecular organometallic catalysts in liquid reaction media, hence contributing to realize the potential of single-atom catalysis to bridge the domains of homogeneous and heterogeneous catalysis.

Conflict of Interest

The authors declare no competing financial interests.

Data Availability Statement

The data that support the findings of this study are available in the Supporting Information of this article.

[1] A. K. Datye, H. Guo, *Nat. Commun.* **2021**, *12*, 895.
[2] S. Mitchell, E. Vorobyeva, J. Pérez-Ramírez, *Angew. Chem. Int. Ed.* **2018**, *57*, 15316–15329; *Angew. Chem.* **2018**, *130*, 15538–15552.
[3] A. Wang, J. Li, T. Zhang, *Nat. Chem. Rev.* **2018**, *2*, 65–81.
[4] J. Jones, H. Xiong, A. T. DeLaRiva, E. J. Peterson, H. Pham, S. R. Challa, G. Qi, S. Oh, M. H. Wiebenga, X. I. Pereira Hernandez, Y. Wang, A. K. Datye, *Science* **2016**, *353*, 150–154.
[5] A. Datye, Y. Wang, *Natl. Sci. Rev.* **2018**, *5*, 630–632.
[6] M. Flytzani-Stephanopoulos, *Acc. Chem. Res.* **2014**, *47*, 783–792.

[7] G. Malta, S. A. Kondrat, S. J. Freakley, C. J. Davies, L. Lu, S. Dawson, A. Thetford, E. K. Gibson, D. J. Morgan, W. Jones, P. P. Wells, P. Johnston, C. R. A. Catlow, C. J. Kiely, G. J. Hutchings, *Science* **2017**, *355*, 1399–1403.

[8] H. Yang, L. Shang, Q. Zhang, R. Shi, G. I. N. Waterhouse, L. Gu, T. Zhang, *Nat. Commun.* **2019**, *10*, 4585.

[9] M. Babucci, F. E. Sarac Oztuna, L. Debefve, A. Boubnov, S. R. Bare, B. C. Gates, U. Unal, A. Uzun, *ACS Catal.* **2019**, *9*, 9905–9913.

[10] Y. Liu, J. C. Liu, T. H. Li, Z. H. Duan, T. Y. Zhang, M. Yan, W. L. Li, H. Xiao, Y. G. Wang, C. R. Chang, J. Li, *Angew. Chem. Int. Ed.* **2020**, *59*, 18586–18590; *Angew. Chem.* **2020**, *132*, 18745–18749.

[11] Q. Wang, X. Huang, Z. L. Zhao, M. Wang, B. Xiang, J. Li, Z. Feng, H. Xu, M. Gu, *J. Am. Chem. Soc.* **2020**, *142*, 7425–7433.

[12] L. Liu, A. Corma, *Chem. Rev.* **2018**, *118*, 4981–5079.

[13] B. B. Sarma, J. Kim, J. Amsler, G. Agostini, C. Weidenthaler, N. Pfänder, R. Arenal, P. Concepción, P. Plessow, F. Studt, G. Prieto, *Angew. Chem. Int. Ed.* **2020**, *59*, 5806–5815; *Angew. Chem.* **2020**, *132*, 5855–5864.

[14] M. M. Millet, G. Algara-Siller, S. Wrabetz, A. Mazheika, F. Girgsdies, D. Teschner, F. Seitz, A. Tarasov, S. V. Levchenko, R. Schlögl, E. Frei, *J. Am. Chem. Soc.* **2019**, *141*, 2451–2461.

[15] H. Qi, J. Yang, F. Liu, L. Zhang, J. Yang, X. Liu, L. Li, Y. Su, Y. Liu, R. Hao, A. Wang, T. Zhang, *Nat. Commun.* **2021**, *12*, 3295.

[16] M. S. Spencer, *J. Catal.* **1985**, *93*, 216–223.

[17] A. Beck, X. Huang, L. Artiglia, M. Zabilskiy, X. Wang, P. Rzepka, D. Palagin, M.-G. Willinger, J. A. van Bokhoven, *Nat. Commun.* **2020**, *11*, 3220.

[18] K. Mudiyanselage, S. D. Senanayake, L. Feria, S. Kundu, A. E. Baber, J. Graciani, A. B. Vidal, S. Agnoli, J. Evans, R. Chang, S. Axnanda, Z. Liu, J. F. Sanz, P. Liu, J. A. Rodriguez, D. J. Stacchiola, *Angew. Chem. Int. Ed.* **2013**, *52*, 5101–5105; *Angew. Chem.* **2013**, *125*, 5205–5209.

[19] T. Choksi, P. Majumdar, J. P. Greeley, *Angew. Chem. Int. Ed.* **2018**, *57*, 15410–15414; *Angew. Chem.* **2018**, *130*, 15636–15640.

[20] J. Kim, B. B. Sarma, E. Andrés, N. Pfänder, P. Concepción, G. Prieto, *ACS Catal.* **2019**, *9*, 10409–10417.

[21] X. I. Pereira-Hernández, A. DeLaRiva, V. Muravev, D. Kunwar, H. Xiong, B. Sudduth, M. Engelhard, L. Kovarik, E. J. M. Hensen, Y. Wang, A. K. Datye, *Nat. Commun.* **2019**, *10*, 1358.

[22] J. Li, Q. Guan, H. Wu, W. Liu, Y. Lin, Z. Sun, X. Ye, X. Zheng, H. Pan, J. Zhu, S. Chen, W. Zhang, S. Wei, J. Lu, *J. Am. Chem. Soc.* **2019**, *141*, 14515–14519.

[23] K. Maiti, S. Maiti, M. T. Curnan, H. J. Kim, J. W. Han, *Adv. Energy Mater.* **2021**, *11*, 2101670.

[24] R. Franke, D. Selent, A. Börner, *Chem. Rev.* **2012**, *112*, 5675–5732.

[25] R. Lang, T. Li, D. Matsumura, S. Miao, Y. Ren, Y.-T. Cui, Y. Tan, B. Qiao, L. Li, A. Wang, X. Wang, T. Zhang, *Angew. Chem. Int. Ed.* **2016**, *55*, 16054–16058; *Angew. Chem.* **2016**, *128*, 16288–16292.

[26] J. Amsler, B. B. Sarma, G. Agostini, G. Prieto, P. N. Plessow, F. Studt, *J. Am. Chem. Soc.* **2020**, *142*, 5087–5096.

[27] Y. Nakajima, S. Shimada, *RSC Adv.* **2015**, *5*, 20603–20616.

[28] P. Gao, G. Liang, T. Ru, X. Liu, H. Qi, A. Wang, F.-E. Chen, *Nat. Commun.* **2021**, *12*, 4698.

[29] D. N. Gorbunov, M. V. Terenina, Y. S. Kardasheva, A. L. Maksimov, E. A. Karakhanov, *Pet. Chem.* **2017**, *57*, 1137–1140.

[30] W. J. Tenn, R. C. Singley, B. R. Rodriguez, J. C. DellaMea, *Catal. Commun.* **2011**, *12*, 1323–1327.

[31] V. I. Zapirtan, B. L. Mojet, J. G. van Ommen, J. Spitzer, L. Lefferts, *Catal. Lett.* **2005**, *101*, 43–47.

[32] Z. Mao, Z. Xie, J. G. Chen, *ACS Catal.* **2021**, *11*, 14575–14585.

[33] L. Alvarado Rupflin, J. Mormul, M. Lejkowski, S. Titlbach, R. Papp, R. Gläser, M. Dimitrakopoulou, X. Huang, A.

[34] S. Hanf, L. Alvarado Rupflin, R. Gläser, S. A. Schunk, *Catalysts* **2020**, *10*, 510.

[35] A. Riisager, R. Fehrmann, M. Haumann, P. Wasserscheid, *Eur. J. Inorg. Chem.* **2006**, 695–706.

[36] H. N. T. Ha, D. T. Duc, T. V. Dao, M. T. Le, A. Riisager, R. Fehrmann, *Catal. Commun.* **2012**, *25*, 136–141.

[37] A. Weiß, M. Giese, M. Lijewski, R. Franke, P. Wasserscheid, M. Haumann, *Catal. Sci. Technol.* **2017**, *7*, 5562–5571.

[38] B. B. Sarma, P. N. Plessow, G. Agostini, P. Concepción, N. Pfänder, L. Kang, F. R. Wang, F. Studt, G. Prieto, *J. Am. Chem. Soc.* **2020**, *142*, 14890–14902.

[39] Y. Hinuma, T. Toyao, T. Kamachi, Z. Maeno, S. Takakusagi, S. Furukawa, I. Takigawa, K. Shimizu, *J. Phys. Chem. C* **2018**, *122*, 29435–29444.

[40] J. Yin, J. Jin, M. Lu, B. Huang, H. Zhang, Y. Peng, P. Xi, C.-H. Yan, *J. Am. Chem. Soc.* **2020**, *142*, 18378–18386.

[41] H. Gu, X. Liu, X. Liu, C. Ling, K. Wei, G. Zhan, Y. Guo, L. Zhang, *Nat. Commun.* **2021**, *12*, 5422.

[42] M. Hübner, D. Koziej, M. Bauer, N. Barsan, K. Kvashnina, M. D. Rossell, U. Weimar, J.-D. Grunwaldt, *Angew. Chem. Int. Ed.* **2011**, *50*, 2841–2844; *Angew. Chem.* **2011**, *123*, 2893–2896.

[43] V. Ortalan, A. Uzun, B. C. Gates, N. D. Browning, *Nat. Nanotechnol.* **2010**, *5*, 843–847.

[44] S. Porter, A. Datye, *Microsc. Microanal.* **2021**, *27*, 2608–2610.

[45] L. Liu, U. Díaz, R. Arenal, G. Agostini, P. Concepción, A. Corma, *Nat. Mater.* **2017**, *16*, 132–138.

[46] L. S. Kibis, A. I. Stadnichenko, S. V. Koscheev, V. I. Zaikovskii, A. I. Boronin, *J. Phys. Chem. C* **2016**, *120*, 19142–19150.

[47] T. Yamagishi, S. Ito, K. Tomishige, K. Kunimori, *Catal. Commun.* **2005**, *6*, 421–425.

[48] I. Ro, M. Xu, G. W. Graham, X. Pan, P. Christopher, *ACS Catal.* **2019**, *9*, 10899–10912.

[49] F. Solymosi, M. Pasztor, *J. Phys. Chem.* **1985**, *89*, 4789–4793.

[50] K. I. Hadjiivanov, G. N. Vayssilov, *Advances in Catalysis, Vol. 47*, Academic Press, New York, **2002**, pp. 307–511.

[51] J. T. Yates, Jr., T. M. Duncan, S. D. Worley, R. W. Vaughan, *J. Chem. Phys.* **1979**, *70*, 1219–1224.

[52] J. P. Perdew, K. Burke, M. Ernzerhof, *Phys. Rev. Lett.* **1996**, *77*, 3865–3868.

[53] S. Grimme, J. Antony, S. Ehrlich, H. Krieg, *J. Chem. Phys.* **2010**, *132*, 154104.

[54] G. Kresse, D. Joubert, *Phys. Rev. B* **1999**, *59*, 1758–1775.

[55] L. Li, Z.-J. Zhao, C. Hu, P. Yang, X. Yuan, Y. Wang, L. Zhang, L. Moskaleva, J. Gong, *ACS Energy Lett.* **2020**, *5*, 552–558.

[56] G. Li, S. Li, Z.-K. Han, C. Zou, H. Wu, W. Yuan, B. Zhu, Y. Gao, H. Yang, Z. Zhang, Y. Wang, *Nano Lett.* **2021**, *21*, 7309–7316.

[57] M. Batzill, K. Katsiev, J. M. Burst, U. Diebold, A. M. Chaka, B. Delley, *Phys. Rev. B* **2005**, *72*, 165414.

[58] M. Sparta, K. J. Børve, V. R. Jensen, *J. Am. Chem. Soc.* **2007**, *129*, 8487–8499.

[59] S. Lee, A. Patra, P. Christopher, D. G. Vlachos, S. Caratzoulas, *ACS Catal.* **2021**, *11*, 9506–9518.

[60] P. Baraneedharan, S. Imran Hussain, V. P. Dinesh, C. Siva, P. Biji, M. Sivakumar, *Appl. Surf. Sci.* **2015**, *357*, 1511–1521.

[61] X. Wang, X. Wang, Q. Di, H. Zhao, B. Liang, J. Yang, *Materials* **2017**, *10*, 1398.